Performance of hollow-core FRP–concrete–steel bridge columns subjected to vehicle collision

Omar I. Abdelkarim, Mohamed A. ElGawady *

Dept. of Civil, Architectural, and Environmental Engineering, Missouri University of Science and Technology, Rolla, MO 65401, United States

ARTICLE INFO

ABSTRACT

This paper presents the behavior of an innovative accelerated bridge construction system of hollow-core fiber-reinforced polymer–concrete–steel (HC-FCS) columns under vehicle collisions using LS-DYNA software. The HC-FCS column consists of a concrete wall sandwiched between an outer fiber-reinforced polymer (FRP) tube and an inner steel tube. The steel tube works as a longitudinal and transverse reinforcement, and the FRP tube confines the sandwiched concrete. Detailed finite element analyses were conducted to investigate the effects of 14 different parameters including the concrete material model, the unconfined concrete compressive strength (f'_c), the material strain rate, the column height-to-diameter ratio, the column diameter, the FRP confinement ratio, the diameter-to-thickness ratio of the steel tube, the column void ratio, the embedded length of the steel tube, the infilled steel tube, the top boundary conditions, the axial load level, the vehicle's velocity, and the vehicle's mass on both dynamic and static impact forces. The peak dynamic force (PDF) and the equivalent static force (ESF) were investigated. The ESF is defined as the peak of the twenty-five millisecond moving average (PTMSA). The PTMSAs of the investigated columns were compared to the ESF of the American Association of State Highway and Transportation Officials- Load and Resistance Factor Design (AASHTO-LRFD; 2670 kN (600 kips)). The AASHTO-LRFD was found to be non-conservative when the column was collided with a heavy vehicle with a mass of more than 16 tons (35 kips) or a high-speed vehicle with a velocity of more than 112 kph (70 mph).

© 2016 Elsevier Ltd. All rights reserved.

1. Introduction

Very tall concrete bridge columns in seismic areas usually have hollow-core cross-section. The use of hollow-core cross-sections in concrete columns reduces both mass and self-weight, thereby also reducing inertial forces. These columns limit the required dimensions of foundations, consequently lowering construction costs.

A new type of hollow-core column was introduced by Montague [1]. The column consists of a concrete wall sandwiched between two generally concentric steel tubes. These columns have been investigated extensively [2–4]. Fiber-reinforced polymer (FRP) tubes have been used repeatedly as an alternative to steel tubes in concrete-filled tube columns. The behavior of concrete-filled FRP tube columns has been investigated under extreme loads [5–13]. More recently, Teng et al. [14] presented a section similar to Montague's [1] but utilizing FRP as an outer tube and steel as an inner tube, developing the hollow-core fiber reinforced polymer–concrete–steel column (HC-FCS). This system combines and optimizes the benefits of all three materials: fiber-reinforced polymer (FRP), concrete, and steel, in addition to the benefits of the hollow-core concrete columns.

Construction of HC-FCS columns revealed several advantages over conventional reinforced concrete (RC) columns. The hollow core of the HC-FCS column uses 60–75% less material and requires 90% less construction time than the conventional solid column [15]. When implemented with a precast construction, it also reduces the freight cost. An HC-FCS column represents a compact engineering system in which the steel and FRP tubes cooperate as stay-in-place formworks, the steel tube acting as both flexural and shear reinforcement. Both tubes provide continuous confinement for the concrete shell, giving it higher strain, strength, and ductility than the concrete of the conventional RC column.

The FRP confinement pressure (f_l) is essential in characterizing the performance of the confined concrete core. Confinement pressure is the lateral pressure exerted by the FRP tube confining the concrete core when the concrete material starts to expand. The confinement pressure and the confinement ratio are calculated as shown below in Eqs. (1) and (2):

* Corresponding author.
E-mail addresses: oiafgc@mail.mst.edu (O.I. Abdelkarim), elgawadym@mst.edu (M.A. ElGawady).

$$\text{Confinement pressure } (f_l) = \frac{2E_f\varepsilon_f t_f}{D} \qquad (1)$$

$$\text{Confinement ratio } (CR) = \frac{f_l}{f_c'} \qquad (2)$$

where E_f is the elastic modulus of the FRP tube in the confinement direction, ε_f is the ultimate tensile strain of the FRP in the confinement direction, t_f is the FRP tube thickness, D is the column's diameter, and f_c' is the characterized unconfined concrete cylindrical strength at 28 days.

HC-FCS columns under axial compression, flexural loading, and a combination of axial compression and flexural loading have been investigated [e.g., 16–23]. The previous studies showed that HC-FCS columns have high flexural strength and displacement ductility. The HC-FCS columns have two modes of failure: steel/concrete compression failure and FRP rupture. The compression failure is a gradual failure combined with steel local buckling, while the FRP rupture is abrupt failure. The HC-FCS column fails by compression failure when the FRP tube provides high confinement, which achieves high lateral drift under flexural loading. The HC-FCS column fails by FRP rupture in the case of thin FRP tubes. According to the writers' best knowledge, no previous studies have investigated HC-FCS columns under vehicle impact loading.

Accidents can have serious repercussions with regard to both human life and transportation systems. Throughout the U.S., vehicles colliding with bridge piers have frequently resulted in partial or complete bridge collapse [24–26]. Lee et al. [27] stated that vehicle collision was the third cause of bridge failures in the United States between the years of 1980 and 2012 because it was the reason for approximately 15% of bridge failures during this period. Numerous researchers have used LS-DYNA [28] software to investigate the modeling of concrete columns under extreme loads such as impact and earthquakes [e.g., 29–32]. In the study of vehicle and bridge column collision, there are two main terms to be calculated: the peak dynamic force (PDF) and the equivalent static force (ESF). The PDF is defined as the maximum contact force between the vehicle and the bridge column. However, no consensus exists among researchers with regard to calculating ESF based on PDF. The ESF represents the design value of the vehicle collision with a bridge column. Abdelkarim and ElGawady [30] concluded, based on extensive study, that the best approach for calculating ESF is the peak of the twenty-five millisecond moving average (PTMSA) of the time-dynamic force relation curve when a vehicle collides with a bridge column.

All of the previous studies examined the behavior of HC-FCS columns under axial, flexural, and combined axial-flexural loading. This paper introduces detailed finite element analyses to investigate the effects of 14 different parameters on both dynamic and static impact forces. Comparisons were also conducted between the ESF of the AASHTO-LRFD [33] (2670 kN [600 kips]) and the PTMSA. In addition, this study presents a comparison between the HC-FCS column and the RC column under vehicle collision.

2. Parametric study

Finite element (FE) modeling of the HC-FCS columns and vehicle collisions with bridge columns were validated in previous studies [17,29]. A comprehensive parametric study was conducted to investigate the behavior of the HC-FCS columns numerically during a vehicle collision. If the bridge pier was not shielded by a crashworthy barrier, the design of the pier must include the collision force. This study investigated unshielded bridge columns under vehicle collision. The distance between the errant vehicle and the unshielded column was 150 mm (0.5 ft). LS-DYNA software was used to examine 14 different parameters, including the following:

- Concrete material model (elastic and nonlinear).
- Unconfined concrete compressive strength (f_c') ranging from 20.7 MPa (3000 psi) to 69.0 MPa (10,000 psi).
- Material strain rate (SR, both considered and not considered).
- Column height-to-diameter ratio (H/D_o) ranging from 2.5 to 10.0.
- Column diameter (D_o) ranging from 1200 mm (4.0 ft) to 2100 mm (7.0 ft).
- The FRP confinement ratio ranging from 0.05 to 0.20.
- Diameter-to-thickness ratio of the inner steel tube ranging from 50 to 200.
- Column void ratio (inner diameter-to-outer diameter ratio) ranging from 0.67 to 0.9.
- Embedded length-to-diameter ratio of the steel tube ranging from 1.0 to 2.0.
- Steel tube infilled foam (empty, infilled soft foam, and infilled rigid foam).
- Column top boundary condition (free, superstructure, and hinged).
- Axial load level (P/P_o) ranging from 0% to 10%.
- Vehicle velocity (v_r) ranging from 32 kph (20 mph) to 112 kph (70 mph)
- Vehicle mass (m) ranging from 2 tons (4.4 kips) to 30 tons (65 kips)

Thirty-four columns (from C0 to C33) were investigated. Column C0 was used as a reference column. The range of selected variables for the columns with regard to the examined parameters is summarized in Table 1. It should be noted that some of the selected parameters may be not common in practice. However, they were used to fully understand the column's performance under a wide spectrum of parameters. One parameter was investigated in each group, and the rest were kept constant as in the reference column. For example, the parameter of column void ratio changed by changing the diameter of the inner steel tube. As a result, the steel tube thickness changed to result in the same diameter-to-thickness ratio.

2.1. Geometry and FE columns modeling

The HC-FCS column consisted of an outer glass FRP tube, an inner steel tube, and concrete sandwiched between them. The inner steel tube was extended inside the footing using an embedded length (L_e), while the FRP tube was stopped at the top of the footing. The steel tube was hollow inside. None of the columns included any shear or flexure reinforcement except the steel tube. The columns investigated in this study were supported on a concrete footing that had a fixed boundary at its bottom.

Fig. 1 illustrates the "C0" reference column components. The reference column had an outer diameter (D_o) of 1500 mm (5.0 ft). It had an inner steel tube with a diameter (D_i) of 1200 (47.2 in.) and a thickness of 26.7 mm (1.05 in.) with a diameter-to-thickness ratio (D_i/t_s) of 45. The column void ratio, or the inner-diameter-to-outer-diameter ratio, was 0.8. The embedded length of the steel tube inside the footing (L_e) was 1800 mm (70.9 in.), representing 1.5 D_i. The thickness of the outer FRP tube was 5.9 mm (0.23 in.) with a confinement ratio of 0.1. The column's height was 7620 mm (25.0 ft) with a height-to-diameter ratio (H/D_o) of 5.0. The soil depth above the top of the footing (d_s) was 1000 mm (3.3 ft). The unconfined concrete cylindrical compressive strength (f_c') was 34.5 MPa (5000 psi). An axial load (P) was applied on the column representing 5% of P_o where P_o is the axial load capacity of the reinforced concrete solid-cross-sectional column that had the same diameter as the HC-FCS column and had

Table 1
Summary of the examined columns' parameters.

Column	Concrete Material	f'_c, MPa (psi)	SR	H/D_o	D_o, m (ft)	CR	D_i/t_s steel tube ratio	Void ratio (D_i/D_o)	Steel Tube embedded length (L_e/D_i)	Steel tube infilled	Top Boundary Condition	Axial load level of P_o	V_c, kph (mph)	m, ton (kip)
C0	Nonlinear	34.5 (5,000)	C	5	1.5 (5)	0.1	75	0.8	1.5	Empty	Hinged	5%	80 (50)	8 (18)
C1	Elastic													
C2	Nonlinear	20.7 (3,000)												
C3		48.3 (7,000)												
C4		69.0 (10,000)												
C5		34.5 (5,000)	N.C.											
C6			C	2.5										
C7				10										
C8				5	1.2 (4)									
C9					1.8 (6)									
C10					2.1 (7)									
C11					1.5 (5)	0.05								
C12						0.15								
C13						0.2								
C14						0.1	50							
C15							100							
C16							150							
C17							200							
C18							75	0.67						
C19								0.9						
C20								0.8	1					
C21									2					
C22									1.5	Soft foam				
C23										Rigid foam				
C24										Empty	Free Superstructure			
C25														
C26											Hinged	0%		
C27												10%		
C28												5%	112 (70)	
C29													56 (35)	
C30													32 (20)	
C31													80 (50)	2 (4.4)
C32														16 (35)
C33														30 (65)

D_o = column diameter, D_i = steel tube diameter, H = column height, L_e = steel tube embedded length, CR = FRP confinement ratio, SR = strain rate, NC = Not Considered, C = Considered, v_r = vehicle velocity, m = vehicle mass.
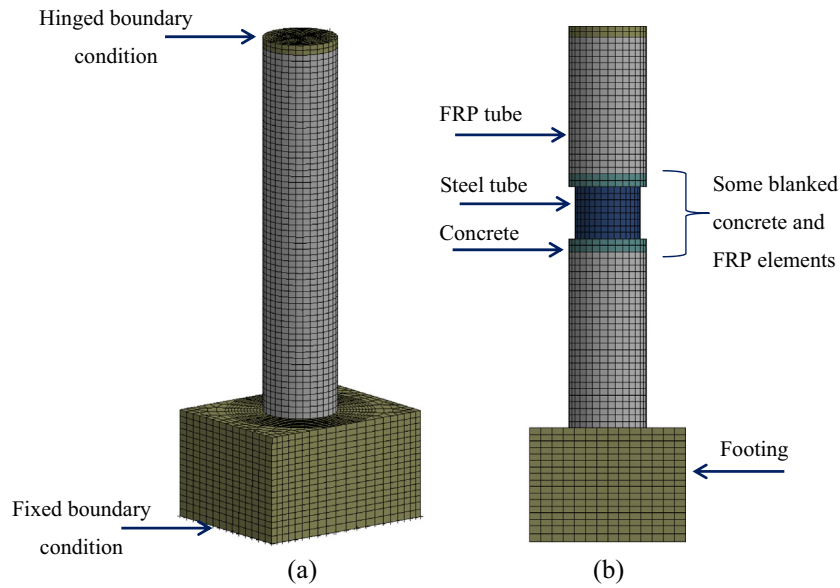
Fig. 1. FE model of the bridge column "C0" for the parametric study: (a) 3D-view and (b) detailed side view of the column components.

1% of longitudinal reinforcements. The P_o was calculated as follows [34]:

$$P_o = A_s f_y + 0.85 f'_c (A_c - A_s) \qquad (3)$$

where A_s = the cross-sectional area of the longitudinal reinforcement of the reinforced concrete solid-cross-sectional column that had the same diameter as the HC-FCS column, A_c = the cross sectional area of the concrete column, f_y = the yield stress of the steel tube, and f'_c = the cylindrical concrete's unconfined compressive stress.

All of the columns except C24 and C25 were hinged at the top ends. Column C24 was free at the top end, while column C25 had a superstructure attached at its top. The bridge superstructure, presented by El-Tawil et al. [35], was comprised of a composite steel-concrete box girder. Thirty-six Belytschko–Schwer resultant beam-type (ELFORM_2) elements were used to simulate two adjacent steel girders (Fig. 2). This superstructure's transformed steel cross-sectional area was 80,000 mm² (124 in.²). The strong moment of inertia (the I_{yy} about the vertical axis) was 8.3×10^{10} mm⁴ (2.0×10^5 in.⁴), and the weak moment of inertia (the I_{zz} about the horizontal axis) was 2.8×10^{10} mm⁴ (6.7×10^4 in.⁴). The superstructure's two unequal spans were 53,340 mm (175 ft) and 50,290 mm (165 ft), respectively. This superstructure was assumed to be pinned at the far ends. The Hughes–Liu beam-type element (ELFORM_2) was used to simulate the bridge bearings located under the superstructure. These bearings were 37 mm (1.5 in.) thick and 200 mm × 200 mm (8

in. × 8 in.) in the cross-section. The bridge bearing's shear modulus was 0.61 MPa (88.0 psi).

One-point quadrature solid elements were used to model each column's concrete core. This type of element assumes constant stress through the element and determines the element's local deformations using an hourglass control. An hourglass control was used to avoid spurious singular modes (e.g., hourglass modes). The hourglass value for each of the models was taken as the default value of 0.10 with an hourglass control type_4 (Flanagan–Belytschko stiffness form). The hourglass controls are the zero-energy deformation modes associated with the one-point-quadrature element that result in a non-constant strain field in the element. Hourglass type 4 constructs geometry-dependent hourglass shape vectors that are orthogonal to the fully linear velocity field and rigid body field (Flanagan and Belytschko). The equations for calculating the vectors are described in the LS-DYNA theory manual. With these vectors they resist the hourglass velocity deformation. This type of hourglass is recommended for structural problems. The implementation of the fully integrated element is very similar to the implementation of the one point by Flanagan and Belytschko, but the hourglass control type 4 is much faster. A rigid cylinder that was 200 mm (7.9 in.) in height, modeled by solid elements, was placed atop the column to avoid excessive local damage to the column's top when the axial loads were applied. Solid elements were used to model the concrete footing.

A surface-to-surface type contact element was used to simulate the interface between the concrete column and the FRP tube. These
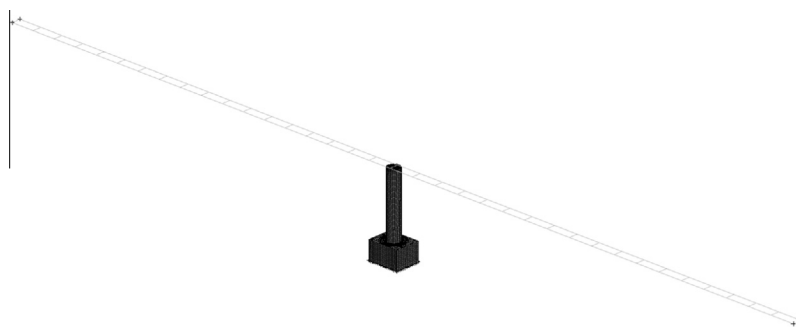

Fig. 2. 3-D view of the column C25 with superstructure.

elements were also used between the concrete column and the steel tube and between the foam inside the steel tube and the steel tube. This type of contact considers the slip and separation that occur between master and slave contact pairs. Hence, slip/debonding is displayed if either occurs between the concrete wall's surface and the tube's surface. This type of contact was also used between the concrete footing and the steel tube. Node-to-surface contact elements were used between the bottom edges of the FRP and steel tubes and the concrete footing. The coefficient of friction for all of the contact elements was taken as 0.6 [17].

2.2. Concrete material models

The AASHTO-LRFD considers vehicle impact to be an extreme load. Therefore, a column's nonlinear behavior is both expected and allowed. Hence, a nonlinear concrete material model (mat72RIII) was used for all columns and footings in this study except Column C1. Mat72RIII was investigated in previous studies for vehicle collision with reinforced concrete bridge columns [31]. Given f'_c and ω, the yield failure surfaces of this model were generated automatically. The fractional dilation parameter (ω) that takes into consideration any volumetric change occurring in the concrete was taken as the default value of 0.50 [17].

The loading strain rate may play an essential role in a structure's response. The dynamic increase factor (DIF) is typically used to describe the increase in concrete strength under dynamic loading as compared to static loading [36–39]. Malvar and Ross [36] modified the CEB [40] model code for use with strain rate effects as in Eqs. (4)–(11). They implemented these equations into an LS-DYNA format.

$$\text{DIF}_c = \frac{f_c}{f_{cs}} = \left(\frac{\dot{\varepsilon}}{\dot{\varepsilon}_s}\right)^{1.026\alpha_s} \quad \text{for } \dot{\varepsilon} \leqslant 30 \text{ s}^{-1} \tag{4}$$

$$\text{DIF}_c = \frac{f_c}{f_{cs}} = \gamma_s \left(\frac{\dot{\varepsilon}}{\dot{\varepsilon}_s}\right)^{0.33} \quad \text{for } \dot{\varepsilon} \leqslant 30 \text{ s}^{-1} \tag{5}$$

$$\alpha_s = \left(5 + 9\frac{f_{cs}}{f_{co}}\right)^{-1} \tag{6}$$

$$\log \gamma_s = 6.156\alpha_s - 2 \tag{7}$$

where DIF_c = compressive strength dynamic increase factor
$\dot{\varepsilon}$ = strain rate in the range of 30×10^{-6}–300 s^{-1},
$\dot{\varepsilon}_s$ = static strain rate of $30 \times 10^{-6} \text{ s}^{-1}$,
f_c = the dynamic compressive strength at $\dot{\varepsilon}$,
f_{cs} = the static compressive strength at $\dot{\varepsilon}_s$,
f_{co} = 10 MPa = 1450 psi.

$$\text{DIF}_t = \frac{f_t}{f_{ts}} = \left(\frac{\dot{\varepsilon}}{\dot{\varepsilon}_s}\right)^{\delta} \quad \text{for } \dot{\varepsilon} \leqslant 1 \text{ s}^{-1} \tag{8}$$

$$\text{DIF}_t = \frac{f_t}{f_{ts}} = \beta \left(\frac{\dot{\varepsilon}}{\dot{\varepsilon}_s}\right)^{0.33} \quad \text{for } \dot{\varepsilon} > 1 \text{ s}^{-1} \tag{9}$$

$$\delta = \left(1 + 8\frac{f_{cs}}{f_{co}}\right)^{-1} \tag{10}$$

$$\log \beta = 6\delta - 2 \tag{11}$$

where DIF_t = tensile strength dynamic increase factor
f_t = the dynamic tensile strength at $\dot{\varepsilon}$,
f_{ts} = the static tensile strength at $\dot{\varepsilon}_s$,
$\dot{\varepsilon}$ = strain rate in the range of 10^{-6}–160 s^{-1},
$\dot{\varepsilon}_s$ = static strain rate of 10^{-6} s^{-1}.

This research was conducted to investigate the effects of two different concrete material models, including elastic (mat001) and nonlinear (mat72RIII) models, on the HC-FCS bridge column's response under vehicle impact. The elastic material model was investigated because it permits greater convenience in design. The elastic material was used for the concrete core and footing of Column C1. The elastic modulus and Poisson's ratio are the only parameters required to define an elastic material model. These parameters were also used for the rigid material to identify the sliding interface parameters of the contact elements between the vehicle and the column. The elastic modulus (E) was calculated according to ACI-318 [34] and considered in the dynamic increase factor (DIF) ($E = 4750\sqrt{\text{DIF} * f'_c}$). Poisson's ratio was taken as 0.20 [41].

2.3. Steel tube material model

An elasto-plastic constitutive model (mat003-plastic_kinamatic) was used for the steel tube. The following five parameters were needed to define this material model: the elastic modulus (E), the yield stress, Poisson's ratio, the tangent modulus, and the ultimate plastic strain. These parameters were assigned the following values: 200 GPa (29,000 ksi); 420.0 MPa (60,900 psi); 0.30; 1102 MPa (160 ksi); and 0.12, respectively [42]. Cowper–Symonds's [43] model was adopted (Eq. (12)) to examine the strain rate effect. Parameters p and c were assigned as a means for identifying the strain rate effect. Constants p and c were taken as 5 and 40, respectively [44]. For example, substituting these two constants into Cowper–Symonds's equation at a strain rate of 100 s^{-1} produced a dynamic yield stress that was 2.20 times the static yield stress. The elastic modulus of the steel did not change considerably under impact loading [45].

$$f_{yd} = 1 + \left(\frac{\dot{\varepsilon}}{c}\right)^{\frac{1}{p}} \tag{12}$$

where f_{yd} = dynamic yield stress and p and c were taken as 5 and 40, respectively.

2.4. FRP tube material model

The FRP material that was used was modeled as an orthotropic material using "054-enhanced composite damage." This material model simulates the composite material by specifying the various failure criteria in compression, tension, or shear using Chang matrix. There are a number of composite material models available in the LS-DYNA library. However, this material model was selected because it correlated well with experimental results of highway guardrail collision [46]. This material is defined by several engineering constants, elastic modulus (E), shear modulus (G), and Poisson's ratio (PR), in the three principle axes (a, b, and c). The fiber orientation was defined by a vector. In addition, the tension and compression FRP strengths were defined. Table 2 summarizes the properties of the FRP tube referenced by the manufacturer's data sheet.

Broutman and Rotem [47] conducted drop weight tests on both unidirectional and cross-ply E-glass/epoxy composites with different geometries. They found that, under a high loading rate, the composite tensile strength increased by approximately 30% for the unidirectional composites and approximately 45% for the cross-ply composites. However, they also found that the energy absorption produced by the high strain rate created a delamination between laminae.

Gama and Gillespie [48] used LS-DYNA software to investigate the strain rate effects on thick-section FRP plate mechanical prop-

Table 2
FRP tubes properties.

	Axial compression elastic modulus (E_a, GPa (ksi))	Axial ultimate stress (f_{ar}, MPa, (psi))	Hoop elastic modulus (E_h, GPa, (ksi))	Hoop rupture stress (f_{hr}, (psi))
FRP tube	4.7 (677)	83.8 (12,150)	20.8 (3020)	276.9 (40,150)

erties. This study developed four rate parameters namely C_{rate1}, C_{rate2}, C_{rate3}, and C_{rate4} to consider the strain rate effect in calculating the FRP strength, longitudinal Young's modulus, shear moduli, and transverse Young's modulus, respectively. The dynamic properties/static properties could be calculated using Eqs. (13)–(17). C_{rate1} was used for all strength values. C_{rate2} was used for in-plane Young's moduli. C_{rate3} was used for all of the shear moduli, and C_{rate4} was used for the transverse modulus. They found that a close correlation between the experiments and finite element analysis was achieved when $(C_{rate1} = C_{rate3} = C_{rate4}) = 0.03$ and $C_{rate2} = 0.00$. For instance, applying Eqs. (13)–(17) at a strain rate of 104 s^{-1} (common for impact loading) [49], yielded a dynamic tensile strength that was approximately 28% higher than the static tensile strength, which is compatible with the drop weight studies that were presented earlier.

$$E = \frac{\{E_{RT}\}}{\{E_0\}} = 1 + \{C_{rate}\} \ln \frac{\{\dot{\varepsilon}\}}{\dot{\varepsilon}_0} \qquad (13)$$

$$\{E_{RT}\} = \{E1\,E2\,E3\,G12\,G31\,G32\}^T \qquad (14)$$

$$\{\dot{\varepsilon}\} = \{|\dot{\varepsilon}_1||\dot{\varepsilon}_2||\dot{\varepsilon}_3||\dot{\varepsilon}_{12}||\dot{\varepsilon}_{31}||\dot{\varepsilon}_{32}|\}^T \qquad (15)$$

$$\{C_{rate}\} = \{C_{rate1}\,C_{rate2}\,C_{rate4}\,C_{rate3}\,C_{rate3}\,C_{rate3}\}^T \qquad (16)$$

$$\dot{\varepsilon}_0 (reference\ train\ rate) = 1 \text{ s}^{-1} \qquad (17)$$

2.5. Foam material model

The steel tube was infilled with soft and rigid foam in Columns C22 and C23, respectively. A material model of low density foam (mat_057) was used to simulate the foam inside the steel tube. The parameters of this material model are the elastic modulus and stress-strain relationship. The material properties of the soft and rigid foam were collected from Tuwair et al. [50], as shown in Fig. 3.

2.6. FE vehicles modeling

Two vehicle models were used in this study: a Ford reduced model (35,353 elements) single unit truck (SUT) and a detailed
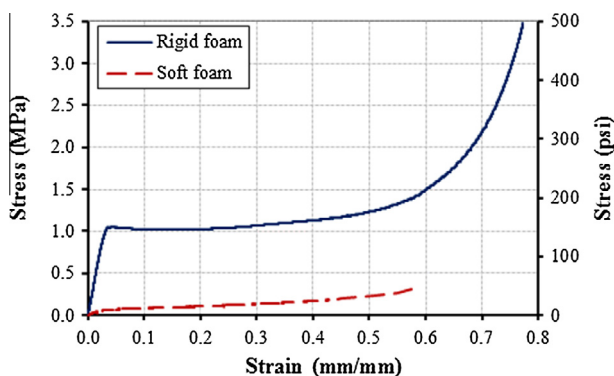

Fig. 3. Stress–strain relationship of the rigid and soft foams [44].

model (58,313 elements) Chevrolet C2500 Pickup (Fig. 4). These models were downloaded from the NCAC website. Experimental tests involving head-on collisions were conducted to validate each model [51,52]. Both models showed high correlation with the experimental results.

Different vehicle speeds were investigated during this research. The vehicle's initial velocities were between 32 kph (20 mph) and 112 kph (70 mph); most had an initial velocity of 80 kph (50 mph). The interface friction between the vehicle and the ground was taken as 0.9. The mass of the vehicle was between 2 tons (4.4 kips) and 30 tons (65 kips); the most was 8 tons (18 kips). The Chevrolet C2500 Pickup was used for the 2-ton (4.4 kips) mass, and the Ford SUT was used for the remaining models. The Ford SUT's mass was changed by changing the cargo mass. Automatic surface-to-surface contact elements by parts, with the contact factor SOFT = 1, were used between the vehicle and the HC-FCS columns [53]. The algorithm Automatic surface-to-surface is penalty-based and was designed to examine each slave node for penetration through the master surface at every time step. Therefore, if any penetration was found between the parts in contact, a nominal interface spring would apply a force proportional to the penetration depth of these interfaces to eliminate the penetration.

3. Results and discussion of the parametric study

3.1. General performance and columns failure

The FE results were reliable when the initial kinetic energy completely transformed into internal energy, hourglass energy, and residual kinetic energy [35]. The hourglass energy was calculated for each model and was lower than 2.5% of the total (Fig. 5). Therefore, the hourglass control did not affect the accuracy of the results. Fig. 6 illustrates the SUT truck's collision with the HC-FCS bridge column "C0" at a time of 0.1 s.

The typical behavior of the time-impact force relationship of the HC-FCS column under vehicle collision is illustrated in Fig. 7. The first peak force occurred when the vehicle's rail collided with the column. The second peak force on the columns, the peak dynamic force (PDF), was produced by the vehicle's engine. The third peak occurred when the vehicle's cargo (in the Ford SUT only) struck the cabinet and the engine. The fourth peak was produced when the rear wheels left the ground. Each of the columns reached their PDF at nearly the same time (40 ms) and had zero impact force beyond 220 ms. The PDF of the reference column "C0" was 3025 kN (680 kips). The PTMSA is the equivalent static force of the impact force, which was calculated as the peak twenty-five millisecond moving average of the time-impact force relation. The PTMSA of Column C0 was 2310 kN (520 kips). The PTMSAs of all of the investigated columns in this study were lower than the equivalent static force of the AASHTO-LRFD of 2670 kN (600 kips), except when the vehicle's velocity was 112 kph (70 mph) and the vehicle's mass was higher than 16 tons (30 kips). Table 3 summarizes the PDF and PTMSA for all of the investigated columns. Fig. 8 illustrates the typical behavior of the frontal and side deformations of the FRP and steel tubes. The difference in the displacement of the FRP and steel tubes, which represents the deformations of the concrete core and FRP tube, was very
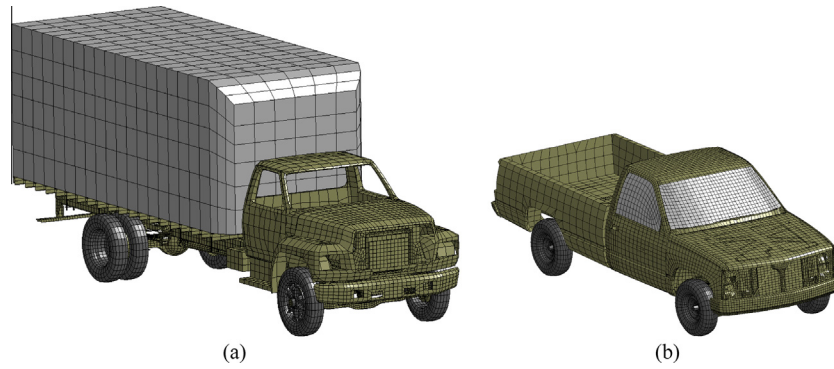
Fig. 4. 3D-view of the FE model: (a) the Ford single unit truck and (b) Chevrolet pickup detailed model.
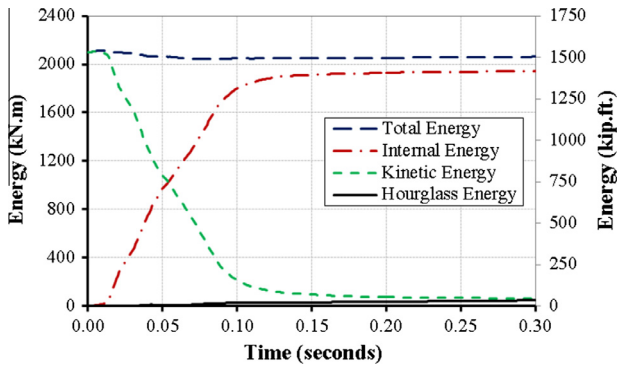

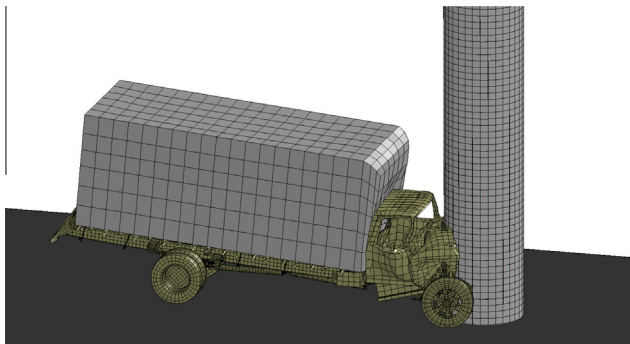**Fig. 5.** Time–energies relations of the FE model C0.

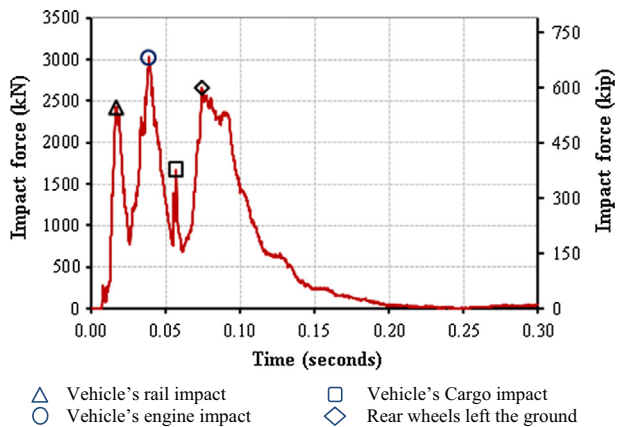**Fig. 6.** Vehicle collision with the HC-FCS column at 0.1 s.

△ Vehicle's rail impact   ☐ Vehicle's Cargo impact
○ Vehicle's engine impact   ◇ Rear wheels left the ground

Fig. 7. Time–impact force of the vehicle collision with the column C0.

low. This behavior indicated that the main resistance of the HC-FCS columns to the vehicle collision came from the inner steel tube. Therefore, none of the investigated columns failed due to FRP rupture.

There is no previous studies on the HC-FCS columns under vehicle collision. Therefore, no consensus exists among researchers with regard to identifying the failure modes of such columns. As the steel tube is the main resistant element of the HC-FCS column under the vehicle collision, the performance of the column was assigned based on the performance of the steel tube. Therefore, the column was assigned "failed, performance level P3" when a significant part of the steel tube ruptured (i.e., the flexural strength reduced by 20%). The column was assigned "operating with damage, performance level P2" when there were residual strains in the tube which means that the column was subjected to permanent damage and might in need to be repaired. Therefore, the performance level P2 was assigned for the investigated columns when the steel tube strains exceeded the yield strain of 2100 microstrain at the location of the collision. While the column was assigned "operating with insignificant damage, performance level P1" when there was no residual strains, i.e., the strains did not exceed the yield strain. For the investigated columns, there was no rupture occurred to any of the columns' steel tubes. Therefore, the columns' performances were defined based on the yield strains. Fig. 9 illustrates the maximum Von Mises strains in the steel tube of each column at the location of the collision. As shown in the figure, four columns (C8, C28, C32, and C33) reached to a performance level P2 under vehicle collision as the maximum strains of their steel tubes exceeded the yield strain which occurred when they were collided with a vehicle had a mass more than 16 tons (35 kips) or was travelling with a speed of 112 kph (70 mph) or when the column diameter was 1.2 m (4 ft).

3.2. Concrete material models

This section investigated the effect of the selected concrete material model on the PDF and PTMSA. Two material models, mat72RIII and mat001, representing nonlinear and elastic behavior, were used for this investigation. Fig. 10(a) illustrates the normalized PDF and PTMSA of the columns with elastic and nonlinear materials. The normalized forces are the PDF and the PTMSA divided by the equivalent static force of the AASHTO-LRFD (2012) of 2670 kN (600 kips). The PDF of Column C1, which was modeled using an elastic material, was approximately 7% higher than that of Column C0, which was modeled using a nonlinear material. This finding was expected as the energy dissipation in the case of the elastic material is lower than that of the nonlinear material. However, this difference in PDF between Columns C0 and C1 was not significant. The reason for that was the effect of the FRP

Table 3
Summary of the FE results.

Variables		Column	Forces		Normalized forces	
Parameter	Value		PDF (kN)	PTMSA (kN)	PDF	PTMSA
Concrete material model	Nonlinear	C0	3027	2310	1.13	0.87
	Elastic	C1	3231	2121	1.21	0.79
f'_c (MPa)	20.7	C2	2840	2250	1.06	0.84
	48.3	C3	3001	2106	1.12	0.79
	69.0	C4	3106	2108	1.16	0.79
Strain rate effect	Not considered	C5	2892	2187	1.08	0.82
Height-to-diameter ratio	2.5	C6	2957	2122	1.11	0.79
	10	C7	3106	2101	1.16	0.79
Column diameter (m)	1.2	C8	3753	2438	1.41	0.91
	1.8	C9	3124	2385	1.17	0.89
	2.1	C10	3137	2193	1.17	0.82
FRP confinement ratio	0.05	C11	2858	2182	1.07	0.82
	0.15	C12	2941	2087	1.10	0.78
	0.20	C13	2979	2204	1.12	0.83
Steel tube D_i/t_s ratio	50	C14	3266	2154	1.22	0.81
	100	C15	2751	2184	1.03	0.82
	150	C16	2755	2292	1.03	0.86
	200	C17	2700	2224	1.01	0.83
Void ratio (D_i/D)	0.67	C18	3439	1998	1.29	0.75
	0.90	C19	2823	2303	1.06	0.86
Steel tube embedded length-to-steel diameter	1.0	C20	2904	2179	1.09	0.82
	2.0	C21	2907	2257	1.09	0.85
Steel tube infilled	Soft foam	C22	2983	2162	1.12	0.81
	Rigid foam	C23	3158	2094	1.18	0.78
Top boundary condition	Free	C24	2853	2310	1.07	0.87
	Superstructure	C25	2882	2172	1.08	0.81
Axial load level	No load	C26	2901	2153	1.09	0.81
	10% of P_o	C27	2963	2177	1.11	0.82
Vehicle velocity (kph)	112	C28	5199	3153	1.95	1.18
	56	C29	2174	1336	0.81	0.50
	32	C30	1752	1316	0.66	0.49
Vehicle mass (ton)	2	C31	3480	1080	1.30	0.40
	16	C32	5152	4532	1.93	1.70
	30	C33	6463	5489	2.42	2.06

confinement, which reduced the nonlinear deformation for the material mat72RIII.

Fig. 11 illustrates that the time-impact load relation of the column with elastic concrete material was steeper than that of the column with nonlinear concrete material. In general, this behavior was because the column response is faster in the case of low deformation than in the case of high deformation. As the PTMSA is an average in a specific time increment, it decreases with steep curves, and vice versa. Therefore, the PTMSA of Column C1, which was modeled using elastic material, was approximately 9% lower than that of Column C0, which was modeled using a nonlinear material. However, this difference in PTMSA between the two columns was not significant. Hence, the study in this section reveals that the elastic material could be used for designing HC-FCS columns under vehicle collision for simplicity.

3.3. Unconfined concrete compressive strength (f'_c)

Four values of f'_c ranging from 20.7 MPa (3000 psi) to 69.0 MPa (10,000 psi), were investigated. Fig. 10(b) illustrates the normalized PDF and PTMSA of the columns with different values of f'_c. The PDF increased by 9%, and the PTMSA decreased by 6%, when the f'_c increased by 233%. This behavior occurred because the high f'_c reduced or delayed the nonlinear deformation that made the curve steeper.

3.4. Strain rate effect

The strain rate effect was included in Column C0 and excluded in Column C5 for all of the column's components. Fig. 10(c) illustrates the normalized PDF and PTMSA of Columns C0 and C5. The PDF and PTMSA did not significantly change considering the strain rate effect. This behavior occurred because the strain rate was considerably low, which would not significantly change the material properties.

3.5. Column height-to-diameter ratio (H/D_o)

Three values of the column height-to-diameter ratio, ranging from 2.5 to 10, were investigated. Fig. 10(d) illustrates the normalized PDF and PTMSA of the columns with different height-to-diameter ratios. The PDF and the PTMSA were almost constant with the changing height-to-diameter ratio. This behavior occurred because the shear forces from the vehicle collision were more dominant rather than flexural as the collision was close to the support.

3.6. Column diameter (D_o)

Four values of the column's diameter, ranging from 1200 mm (4.0 ft) to 2100 mm (7.0 ft), were investigated. Fig. 10(e) illustrates the normalized PDF and PTMSA of the columns with different
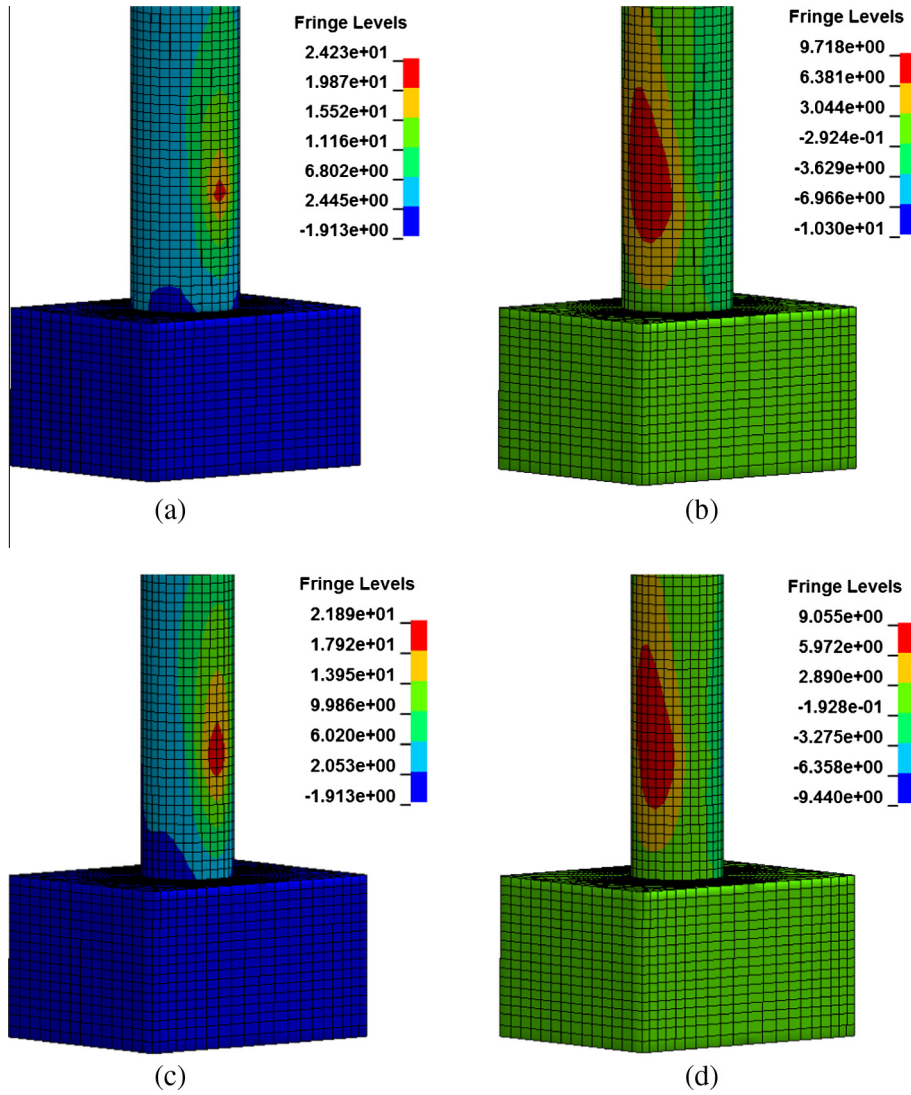
Fig. 8. Column C0 displacement contours of: (a) FRP head-on direction, (b) FRP side direction, (c) steel head-on direction, and (d) steel side direction at time of the PDF of 0.04 s, units are in mm (1 mm = 0.04 in.).
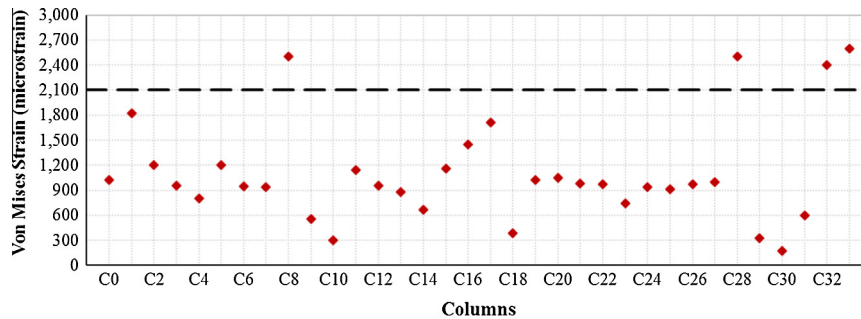

Fig. 9. Maximum Von Mises strains of the steel tubes at the zone of collision.

diameters. The PDF of all of the columns, except for Column C8 with a diameter of 1200 (4.0 ft), was almost constant. The PDF of Column C8, which had a diameter of 1200 mm (4.0 ft), was approximately 25% higher than that of Column C0, which had a diameter of 1500 mm (5.0 ft). This behavior occurred because the steel tube of the low-diameter column, C8, had a high curvature that increased the lateral resistance of the steel tube. Hence, the steel tube deformation decreased and, as a result, the energy dissipation

decreased, leading to a higher PDF. However, the PTMSA was almost constant with the changing column diameter, which agreed with a previous study conducted by Buth et al. [25].

3.7. FRP confinement ratio (f_l/f_c')

Four values of FRP confinement ratios, ranging from 0.05 to 0.2, were investigated. Fig. 10(f) illustrates the normalized PDF and
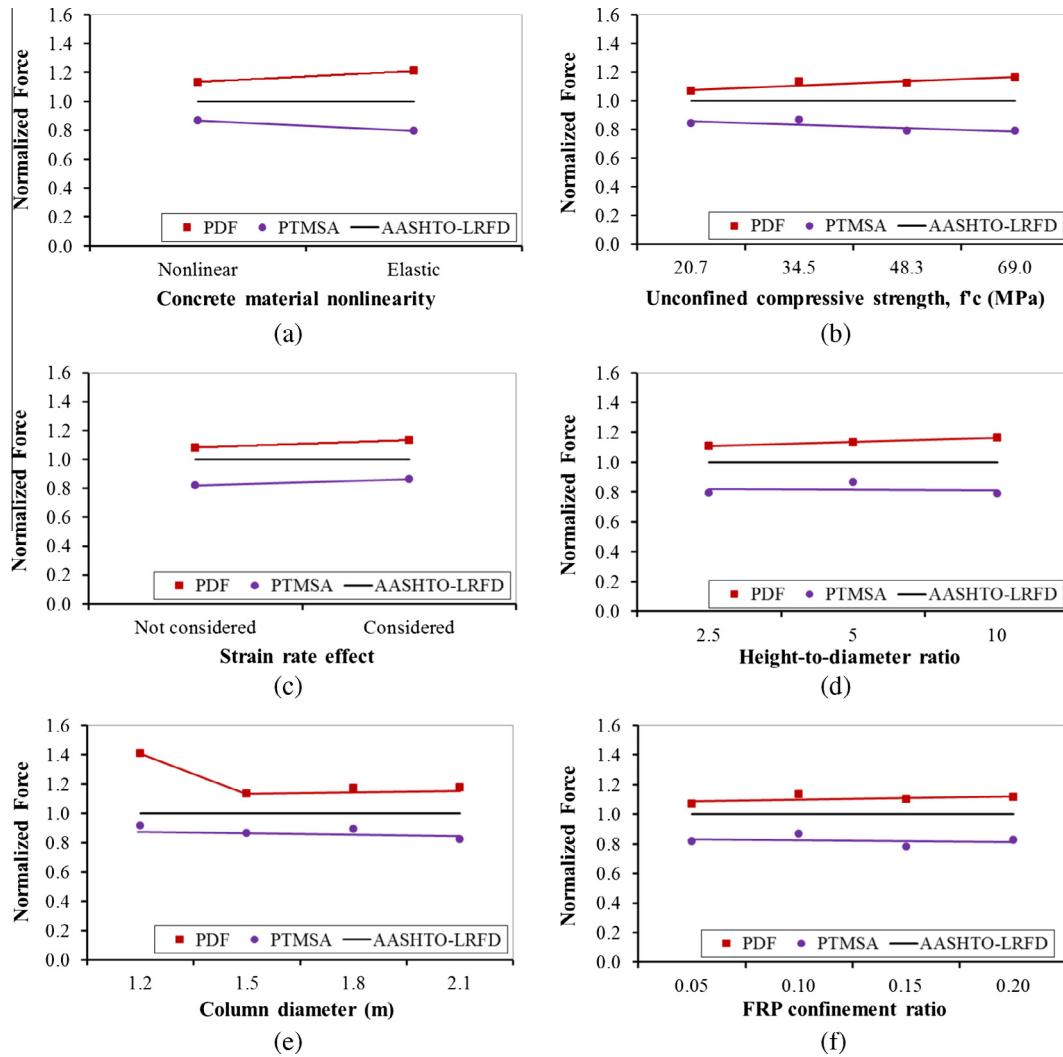
Fig. 10. Effects of (a) concrete material nonlinearity, (b) f'_c, (c) strain rate, (d) height-to-diameter ratio, (e) column diameter, and (f) FRP confinement ratio on PDF and ESF.
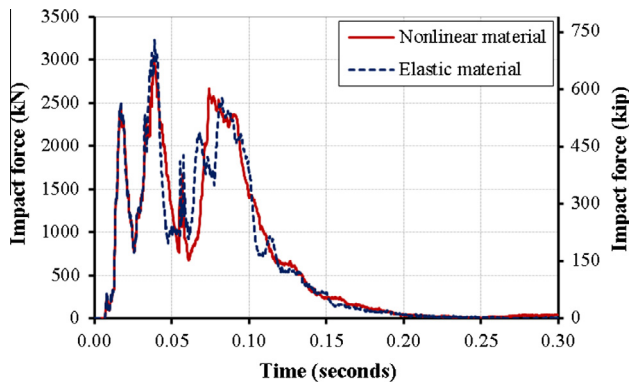

Fig. 11. Time–impact force of the vehicle collision with the columns with concrete nonlinear and linear materials.

PTMSA of the columns with different FRP confinement ratios. The PDF and PTMSA of all of the columns were almost constant with the changing FRP confinement ratio. This behavior occurred because the concrete stress was lower or slightly higher than the f'_c as the main resistance was from the steel tube. Hence, the FRP confinement had almost no effect on the PDF or PTMSA, but it saved the concrete core from spalling.

3.8. Diameter-to-thickness ratio of the steel tube (D_i/t_s)

Five values of diameter-to-thickness (D_i/t_s) ratios for the steel tube, ranging from 50 to 200, were investigated. Fig. 12(a) illustrates the normalized PDF and PTMSA of the columns with different diameter-to-thickness ratios of the steel tube. The PDF decreased nonlinearly by approximately 21% when the D_i/t_s of the steel tube increased by 300%. This behavior occurred because the higher D_i/t_s of the steel tube led to a higher steel tube deformation and a higher energy dissipation. However, the PTMSA was almost constant with the changing D_i/t_s of the steel tube. This behavior occurred because the time-impact load relation of the column with a low D_i/t_s of the steel tube was steeper than that of the column with a high D_i/t_s of the steel tube (Fig. 13).

3.9. Column void ratio (D_i/D_o)

Three values of column void ratios (D_i/D_o), ranging from 0.67 to 0.9, were investigated. Fig. 12(b) illustrates the normalized PDF and PTMSA of the columns with different column void ratios. The PDF decreased nonlinearly by approximately 22% when the column void ratio increased by 34%. This behavior occurred because of the effect of the steel tube curvature. The steel tube was flatter for the case of the high void ratio than that of the low void ratio. Hence, the steel
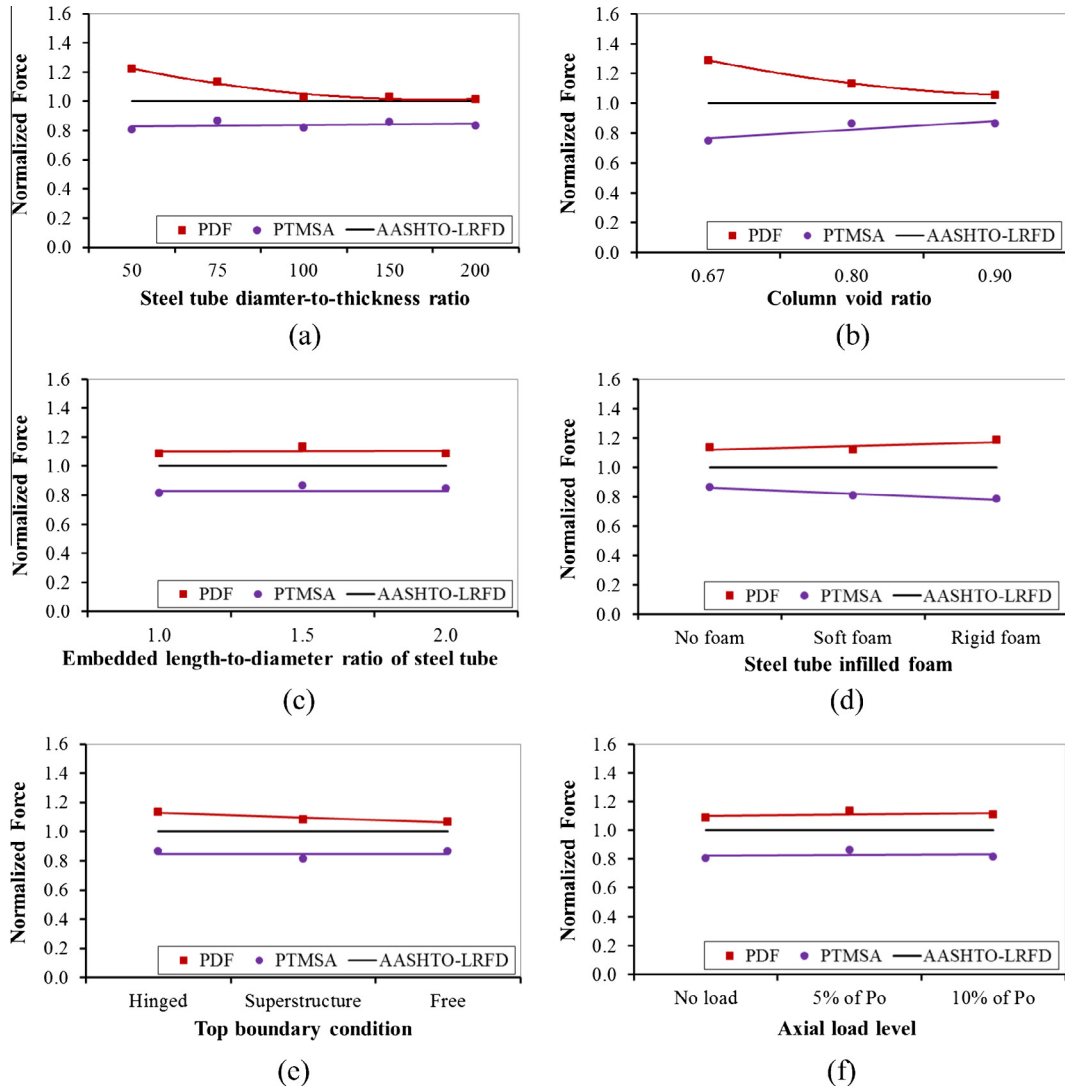
Fig. 12. Effects of (a) steel tube diameter-to-thickness ratio, (b) column void ratio, (c) embedded length-to-diameter ratio of steel tube, (d) steel tube infilled foam, (e) top boundary condition, and (f) axial load level on PDF and ESF.
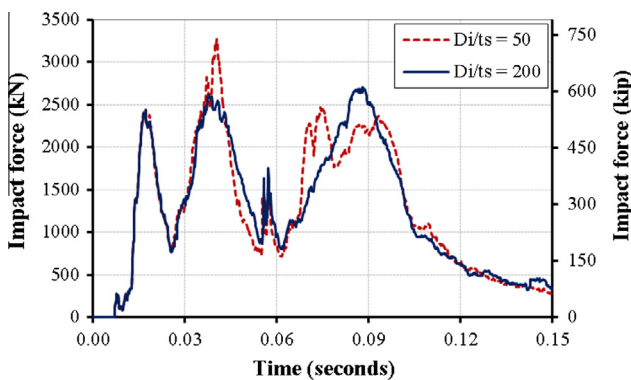

Fig. 13. Time–impact force of the vehicle collision with the columns with concrete high and low diameter-to-thickness ratio of the steel tube.
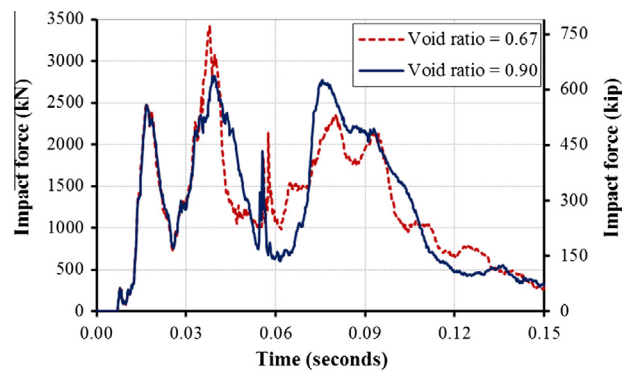

Fig. 14. Time–impact force of the vehicle collision with the columns with concrete high and low column void ratio.

tube deformation increased when the steel tube diameter increased. As a result, the energy dissipation increased, leading to a lower PDF. However, the PTMSA increased almost linearly when the column void ratio increased by 34%. This behavior occurred because the time-impact load relation of the column with a low D_i/D_o was steeper than that of the column with a high D_i/D_o (Fig. 14).

3.10. Embedded length-to-diameter ratio of steel tube (L_e/D_i)

Three values of embedded length-to-diameter (L_e/D_i) ratios of the steel tube, ranging from 1 to 2, were investigated. Fig. 12(c) illustrates the normalized PDF and PTMSA of the columns with
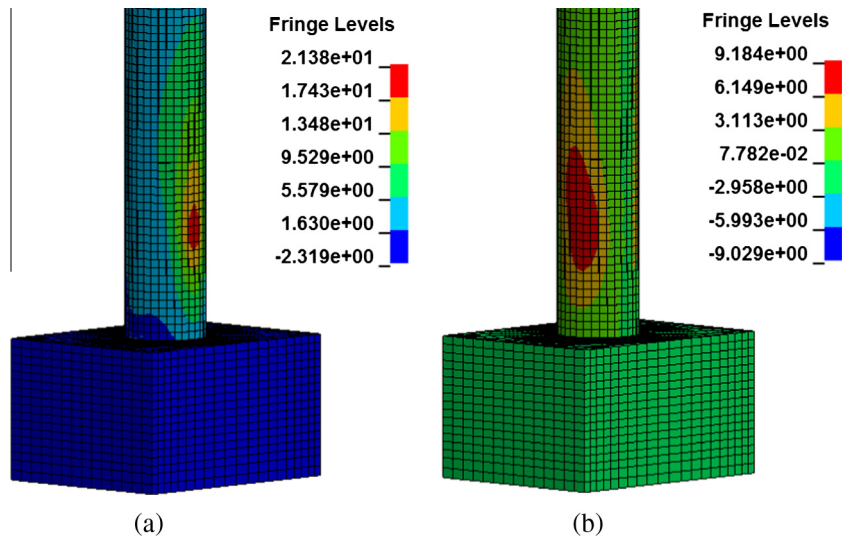
Fig. 15. Column C22, steel tube infilled soft foam, displacement contours of: (a) steel tube-frontal direction and (b) steel tube-side direction at time of the PDF of 0.04 s, units are in mm (1 mm = 0.04 in.).

different column void ratios. The PDF and PTMSA were almost constant with the changing embedded length. This behavior occurred because the shear forces from the vehicle collision were more dominant rather than flexural as the vehicle collision was close to the support.

3.11. Steel tube infilled foam

The steel tube was infilled with soft and rigid foam in Columns C22 and C23, respectively, and the results were compared with those of Column C0, which had an empty steel tube. Fig. 12(d) illustrates the normalized PDF and PTMSA of the columns with different column void ratios. The PDF increased slightly when the steel tube was infilled with foam. This behavior occurred because the infilled foam reduced the steel tube deformation. Figs. 15 and 16 illustrate the frontal and side deformations of the steel tube for the columns with infilled soft and rigid foams, respectively. The frontal deformation of the steel tube was reduced by 3% and 33% when it was infilled with soft and rigid foam, respectively.

The side deformation of the steel tube was reduced by 2.5% and 48% when it was infilled with soft and rigid foam, respectively. This result is in good agreement with the result of previous study on using hard foam in thin-walled hollow steel members in vehicles to increase their strength [54]. The PTMSA decreased when the steel tube was infilled with foam. This behavior occurred because the time-impact load relation of the column with the steel tube infilled with foam was steeper than that of the column with an empty steel tube.

3.12. Top boundary conditions

Three of the column's top boundary conditions, including free, hinged, and superstructure, were investigated. Fig. 12(e) illustrates the normalized PDF and PTMSA of the columns with different top boundary conditions. Changing the column's top boundary condition changed the PDF values slightly because the PDF was induced in a very short period of time. This behavior occurred because the impact loading occurred in a very short time. Hence, the structure
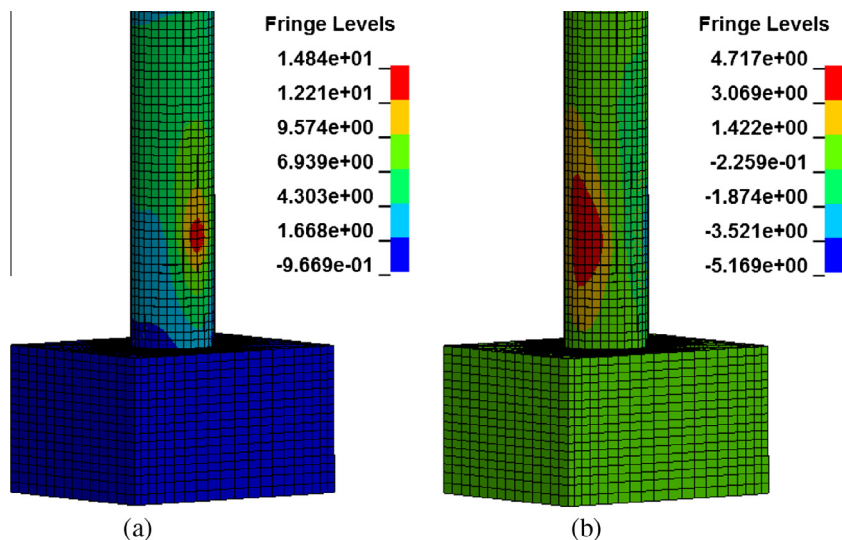

Fig. 16. Column C23, steel tube infilled rigid foam, displacement contours of: (a) steel tube-frontal direction and (b) steel tube-side direction at time of the PDF of 0.04 s, units are in mm (1 mm = 0.04 in.).
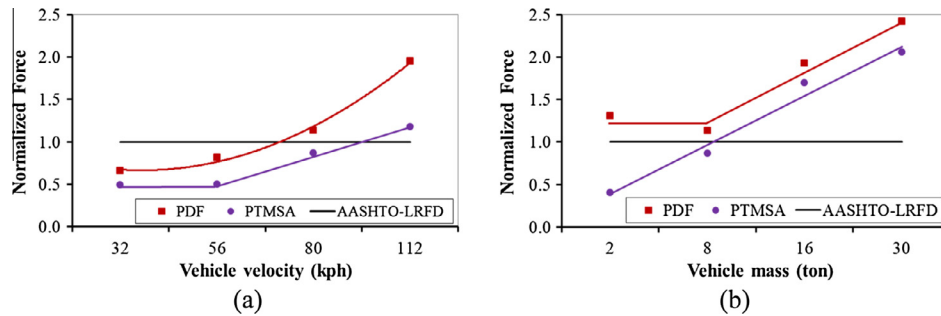
Fig. 17. Effects of (a) vehicle velocity and (b) vehicle mass on PDF and ESF.

did not have enough time to respond. This result is compatible with the study by Chopra [55] on the pulse shape. If the pulse duration is much shorter than the natural period (as in impact loading), the structure's response is mainly controlled by the total kinetic energy. However, the maximum lateral displacement of Column C22, which had a free top boundary condition, was significantly higher than those of Columns C0 and C23, which had hinged and superstructure top conditions, respectively. The existence of the superstructure in Column C23 resulted in a top boundary condition similar to that in Column C0. The PTMSA was almost constant with the column's changing top boundary condition.

3.13. Axial load level

Three values of axial load levels, ranging from 0% to 10% of the axial capacity (P_o) of a reinforced concrete column of the same diameter with a longitudinal reinforcement ratio of 1%, were investigated. Fig. 12(f) illustrates the normalized PDF and PTMSA of the columns with different axial load levels. The PDF and PTMSA were almost constant with the changing axial load level. This behavior occurred because the axial stresses coming from an axial load would mainly be applied on the concrete core with insignificant stresses on the steel tube because the axial stiffness of the concrete core is much higher than that of the steel tube. However, the vehicle collision was mainly resisted by the steel tube. Therefore, the axial load level did not affect the PDF or the PTMSA for the HC-FCS columns.

3.14. Vehicle velocity

Four vehicle velocities, ranging from 32 kph (20 mph) to 112 kph (70 mph), were investigated. Fig. 17(a) illustrates the normalized PDF and PTMSA of the columns with different vehicle velocities. The PDF tended to increase nonlinearly when the vehicle's velocity increased. It is of interest that the increase in the PDF is not proportional to the square of the velocity, as in the case of elastic impact problems. Damage to the columns reduced the rate of increase in the PDF. For example, the PDF increased by approximately 200% when the vehicle's velocity increased from 32 kph (20 mph) to 112 kph (70 mph). The PTMSA increased almost linearly by 140% when the vehicle's velocity increased from 56 kph (35 mph) to 112 kph (70 mph). However, the PTMSA was almost constant when the vehicle's velocity increased from 32 kph (20 mph) to 56 kph (35 mph) because the kinetic energy of both cases was considerable. The AASHTO-LRFD under-predicted the equivalent static force when the column was collided with by a high-speed vehicle at a velocity of 112 kph (70 mph). The PTMSA was almost 1.2 times the equivalent static force of the AASHTO-LRFD of 2670 kN (600 kips) when the column was collided with by a high-speed vehicle at a velocity of 112 kph (70 mph).

3.15. Vehicle mass

Four vehicle masses, ranging from 2 tons (4.4 kips) to 30 tons (65 kips), were investigated. Fig. 17(b) illustrates the normalized PDF and PTMSA of the columns with different vehicle velocities. In general, both the PDF and ESF increased linearly when the vehicle's mass increased. However, the rate of increase was slower than anticipated in elastic impact problems. For example, the PDF increased by approximately 86% when the vehicle's mass increased from 2 tons (4.4 kips) to 30 tons (65 kips). The PDF barely changed when the vehicle's mass increased from 2 tons (4.4 kips) to 8 tons (18 kips) because the energy dissipation, in the form of inelastic deformations, whether in the vehicle or in the column, did not significantly change as the kinetic energy was not considerably high. The PTMSA increased almost linearly by approximately 410% when the vehicle mass increased from 2 tons (4.4 kips) to 30 tons (65 kips). The AASHTO-LRFD under-predicted the equivalent static force when the column was collided with by the heavy vehicle with a mass greater than 16 tons (35 kips). The PTMSA was almost 2.1 times the equivalent static force of the AASHTO-LRFD of 2670 kN (600 kips) when the column was collided with by a heavy vehicle with a mass of 30 tons (65 kips).

4. ESF equation for HC-FCS columns under vehicle collision

Based on the presented parametric study, the PTMSAs of the columns were studied mathematically using CurveExpert Professional software, and SAS software to introduce a design equation for estimating kinetic-energy based ESF (KEB$_{ESF}$) which was presented in Eq. (18). Fig. 18 illustrates the relation between the vehicle's kinetic energy and the normalized PTMSA and the normalized
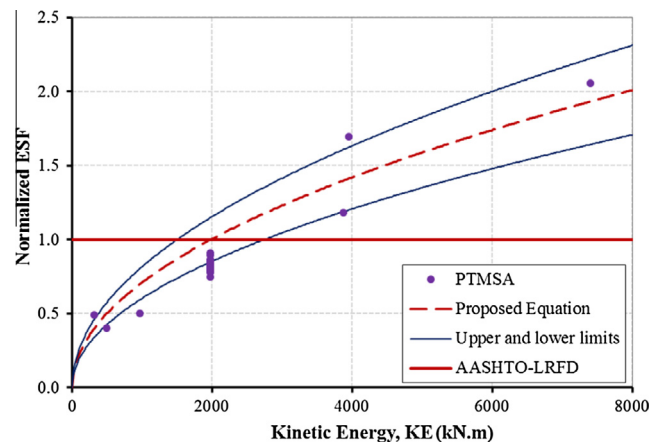

Fig. 18. The ESF proposed equation versus the FE results based on the kinetic energy.
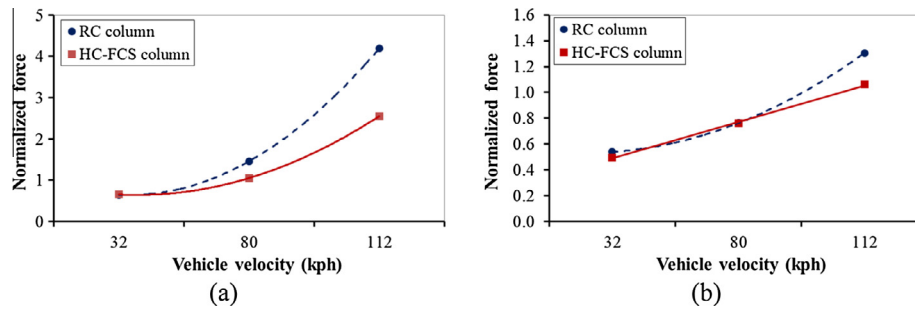
Fig. 19. The HC-FCS versus RC columns at different vehicle's velocities: (a) PDF and (b) PTMSA.

KEB_{ESF} as well. Both the upper and lower limits (referring to ±15% of the KEB_{ESF}) are also depicted in Fig. 18. The proposed KEB_{ESF} equation well correlated with the FE results.

$$KEB_{ESF} = 42\sqrt{mv_r^2} = 60\sqrt{KE} \qquad (18)$$

where m = the vehicle mass in ton, v_r = the vehicle velocity in m/s, and KE = kinetic energy of the vehicle in kN m.

5. Comparison between HC-FCS and RC Columns under different velocities

Column C16 was compared, under vehicle collision, with an RC column with the same flexural strength. Both columns had the superstructure of Column C25. The longitudinal steel reinforcement of the RC column was 24 D35 (24 #11), representing up to 1.25% of the concrete cross-sectional area. The RC column's hoop reinforcement was 5 D16 (5 #5). Modeling of the RC column was explained by Abdelkarim and ElGawady [29]. The RC and HC-FCS columns were collided with by a Ford F800 single unit truck (SUT) with three different velocities of 112 kph (70 mph), 80 kph (50 mph), and 32 kph (20 mph).

Fig. 19 illustrates the PDF and PTMSA of the investigated columns. The PDF of the HC-FCS column was lower than that of the RC column by approximately 40% and 28% when it was collided with by a vehicle with a velocity of 112 kph (70 mph) and 80 kph (50 mph), respectively (Fig. 19a). However, the PDFs of the HC-FCS and RC columns were almost the same when they were collided with by a vehicle travelling with a velocity of 32 kph (20 mph). The PTMSA of the HC-FCS column was lower than that of the RC column by approximately 20% when it was collided with by a vehicle with a velocity of 112 kph (70 mph) (Fig. 19b). However, the PTMSAs of the HC-FCS and RC columns were almost the same when they were collided with by a vehicle travelling with a velocity of 80 kph (50 mph) or 32 kph (20 mph).

The concrete spalling occurred during the vehicle collision with the RC column because of the high local strain. However, the FRP tube in the HC-FCS column protected the concrete from spalling and increased the ultimate compressive strain by approximately 5 times that of the RC column.

6. Conclusions

This paper presented the behavior of the HC-FCS columns under vehicle collision. The two main terms of the study of a vehicle collision with a bridge column are the peak dynamic force (PDF) and the equivalent static force (ESF). These terms were evaluated through an extensive parametric study. The extensive parametric study investigated the effects of 14 different parameters: the concrete material model, the unconfined concrete compressive strength (f'_c), the material strain rate, the column height-to-

diameter ratio, the column diameter, the FRP confinement ratio, the diameter-to-thickness ratio of the steel tube, the column void ratio, the embedded length of the steel tube, the infilled steel tube, the top boundary conditions, the axial load level, the vehicle's velocity, and the vehicle's mass on both dynamic and static impact forces. This study revealed that the main resistance of the HC-FCS columns to the vehicle collision came from the inner steel tube. The elastic properties can be used, for simplicity, to design the HC-FCS columns under vehicle collision. Using a steel tube infilled with a rigid foam and a column with a high void ratio is recommended for the HC-FCS columns to resist the vehicle collision. The PDF of the HC-FCS column was lower than that of the RC column by approximately 40% and 28% when it was collided with by a vehicle at a velocity of 112 kph (70 mph) and 80 kph (50 mph), respectively. The equation $\left(KEB_{ESF} = 42\sqrt{mv_r^2} = 60\sqrt{KE}\right)$ was presented in this paper to estimate the ESF of a vehicle's collision with the HC-FCS bridge columns.

References

[1] Montague P. Experimental behavior of double-skinned, composite, circular cylindrical-shells under external-pressure. J Mech Eng Sci 1978;20(1):21–34.

[2] Fouche P, Bruneau M. Non-linear analysis of multi-hazard performance of cylindrical concrete filled steel tubes bridge piers. In: Proceedings of 8th international conference on short and medium span bridges, Canada, 2010.

[3] Hajjar J. Concrete-filled steel tube columns under earthquake loads. Struct Eng Mater 2000;2(1):72–82.

[4] Shakir-Khalil H, Illouli S. Composite columns of concentric steel tubes. In: Proc., conf. on the design and construction of non-conventional structures. vol. 1. London, 1987. p. 73–82.

[5] Qasrawi Y, Heffernan PJ, Fam A. Performance of concrete-filled FRP tubes under field close-in blast loading. J Compos Constr 2014. http://dx.doi.org/10.1061/(ASCE)CC.1943-5614.0000502. 04014067.

[6] Anumolu S, Abdelkarim O, ElGawady MA. Behavior of hollow-core steel-concrete-steel columns under torsion loads. J Bridge Eng, ASCE 2016. 04016070–1:14.

[7] Youssf O, ElGawady MA, Mills J. Static cyclic behaviour of FRP-confined crumb rubber concrete columns. Eng Struct 2016;113:371–87.

[8] Moustafa A, ElGawady MA. Strain rate effects on conventional and rubberized concrete encased in FRP tubes. J Compos Constr 2016:04016014. http://dx.doi.org/10.1061/(ASCE)CC.1943-5614.0000658.

[9] Abdelkarim O, ElGawady MA. Concrete-filled-large deformable FRP tubular columns under axial compressive loading. Fibers 2015;3:432–49.

[10] Ozbakkaloglu T, Saatcioglu M. Seismic performance of square high-strength concrete columns in FRP stay-in-place formwork. J Struct Eng 2007:44–56. http://dx.doi.org/10.1061/(ASCE)0733-9445(2007) 133:1(44).

[11] Ozbakkaloglu T, Akin E. Behavior of FRP-confined normal- and high-strength concrete under cyclic axial compression. J Compos Constr 2012:451–63. http://dx.doi.org/10.1061/(ASCE)CC.1943-5614.0000273.

[12] Idris Y, Ozbakkaloglu T. Seismic behavior of high-strength concrete-filled FRP tube columns. J Compos Constr 2013. http://dx.doi.org/10.1061/(ASCE) CC.1943-5614.0000388. 04013013.

[13] Ozbakkaloglu T. Compressive behavior of concrete-filled FRP tube columns: assessment of critical column parameters. Eng Struct 2013;51:188–99.

[14] Teng JG, Yu T, Wong YL. Behavior of Hybrid FRP–concrete–steel double-skin tubular columns. In: Proc. 2nd Int. Conf. on FRP composites in civil engineering, Adelaide, Australia, 2004. p. 811–8.

[15] Abdelkarim O, ElGawady MA. Behavior of Hollow FRP-Concrete-Steel Columns under Static Cyclic Axial Compressive Loading. Eng Struct 2016;123:77–88.

[16] Abdelkarim O, ElGawady M. Behavior of hybrid FRP–concrete–steel double-skin tubes subjected to cyclic axial compression. Struct Congress 2014;2014:1002–13.

[17] Abdelkarim O, ElGawady M. Analytical and finite-element modeling of FRP–concrete–steel double-skin tubular columns. J Bridge Eng 2014. http://dx.doi.org/10.1061/(ASCE)BE.1943-5592.0000700. B4014005.

[18] Teng JG, Yu T, Wong YL, Dong SL. Innovative FRP–steel–concrete hybrid columns. Adv Steel Struct 2005;1:545–54.

[19] Fanggi BAL, Ozbakkaloglu T. Square FRP–HSC–steel composite columns: behavior under axial compression. Eng Struct 2015;92:156–71.

[20] Ozbakkaloglu T, Idris Y. Seismic behavior of FRP-high-strength concrete-steel double-skin tubular columns. J Struct Eng 2014. http://dx.doi.org/10.1061/(ASCE)ST.1943-541X.0000981. 04014019.

[21] Idris Y, Ozbakkaloglu T. Flexural behavior of FRP–HSC-steel composite beams. Thin-Walled Struct 2014;80:207–16.

[22] Han LH, Tao Z, Liao FY, Xu Y. Tests on cyclic performance of FRP–concrete–steel double-skin tubular columns. Thin-Walled Struct 2010;48(6):430–9.

[23] Yu T, Wong YL, Dong SL, Lam ESS. Flexural behavior of hybrid FRP–concrete–steel double skin tubular members. J Compos Constr 2006:443–52. http://dx.doi.org/10.1061/(ASCE)1090-0268(2006) 10:5(443).

[24] Harik I, Shaaban A, Gesund H, Valli G, Wang S. United States Bridge Failures, 1951–1988. J Perform Constr Facil 1990;4(4):272–7.

[25] Buth CE, Williams WF, Brackin MS, Lord D, Geedipally SR, Abu-Odeh AY. Analysis of large truck collisions with bridge piers: phase 1. Texas Department of Transportation Research and Technology Implementation Office; 2010. 9-4973-1.

[26] Agrawal AK. Bridge vehicle impact assessment: final report. University transportation research center and New York State Department of Transportation; 2011.

[27] Lee GC, Mohan S, Huang C, Fard BN. A study of US bridge failures (1980–2012). MCEER technical report 13-0008. Buffalo (NY); 2013.

[28] LS-DYNA; theory manual for version 971. Livermore Software Technology Corporation; 2006.

[29] Abdelkarim OI, ElGawady MA. Design of short reinforced concrete bridge columns under vehicle collision. Transp Res Record: J Transp Res B 2016;2592:27–37.

[30] Abdelkarim O, ElGawady M. Vehicle collision with reinforced concrete bridge columns. In: Proceedings of the fifth international workshop on performance, protection & strengthening of structures under extreme loading, Michigan, June 2015. p. 628–35.

[31] Sharma H, Hurlebaus S, Gardoni P. Performance-based response evaluation of reinforced concrete columns subject to vehicle impact. Int J Impact Eng 2012;43:52–62.

[32] Thilakarathna HMI, Thambiratnam DP, Dhanasekar M, Perera N. Numerical simulation of axially loaded concrete columns under transverse impact and vulnerability assessment. Int J Impact Eng 2010;37:1100–12.

[33] AASHTO. AASHTO-LRFD bridge design specifications – customary US units. 6th ed. Washington (DC): AASHTO; 2012.

[34] A.C.I. Committee 318. Building code requirements for structural concrete (ACI318-11) and commentary (318R-11). Farmington Hills, Mich: American Concrete Institute; 2011. p. 509.

[35] El-Tawil S, Severino E, Fonseca P. Vehicle collision with bridge piers. J Bridge Eng 2005;10(3):345–53.

[36] Malvar LJ, Ross CA. Review of strain rate effects for concrete in tension. ACI Mater J 1998;95:735–9.

[37] Bischoff PH, Perry SH. Compressive behavior of concrete at high strain rates. Mater Struct 1991;24:425–50.

[38] Williams MS. Modeling of local impact effects on plain and reinforced concrete. ACI Struct J 1994;91(2):178–87.

[39] Fu HC, Erki MA, Seckin M. Review of effects of loading rate on reinforced concrete. J Struct Eng 1991;117(12):3660–79.

[40] Comité Euro-International du Béton. CEB-FIP Model Code 1990. Trowbridge (Wiltshire, UK): Redwood Books; 1993.

[41] Mehta KP, Monteiro PJM. CONCRETE: microstructure, properties, and materials. 3rd ed. United States of America: McGraw-Hill Inc.; 2006. p. 660.

[42] California department of transportation. Seismic Design Criteria. California Department of Transportation, Rev. 1.4, 2006.

[43] Cowper GR, Symonds PS. Strain hardening and strain rate effects in impact loading of cantilever beams. Brown University, App. Math. Report No. 28, 1957.

[44] Yan X, Yali S. Impact behaviors of CFT and CFRP confined CFT stub columns. J Compos Constr 2012;16(6):662–70.

[45] Campbell JD. The yield of mild steel under impact loading. J Mech Phys Solids 1954;3:54–62.

[46] Bank LC, Gentry TR. Development of a pultruded composite material highway guardrail. Compos A Appl Sci Manuf 2001;32(9):1329–38.

[47] Broutman LJ, Rotem A. Impact strength and toughness of fiber composite materials. Foreign object impact damage to composites; 1975. p. 114–33.

[48] Gama BA, Gillespie JW. Finite element modeling of impact, damage evolution and penetration of thick-section composites. Int J Impact Eng 2011;38(4):181–97.

[49] Sierakowsi RL, Chaturved SK. Dynamic loading and characterization of fiber-reinforced composites. New York (USA): John Wiley & Sons Inc; 1997.

[50] Tuwair H, Hopkins M, Volz J, ElGawady MA, Mohamed M, Chandrashekhara K, Birman V. Evaluation of sandwich panels with various polyurethane foam-cores and ribs. Compos B Eng 2015;79:262–76.

[51] Mohan P, Marzougui D, Kan C. Validation of a single unit truck model for roadside hardware impacts. NCAC, the George Washington University; 2003.

[52] Zaouk AK, Bedewi NE, Kan CD, Marzoughi D. Evaluation of a multi-purpose pick-up truck model using full scale crash data with application to highway barrier impact. In: 29th Inter. Sym. on Auto. Tech. and Auto., Florence, Italy, 1996.

[53] Bala S. Contact Modeling in LS-DYNA. Livermore Software Technology Corporation; 2001.

[54] Lilley K, Mani A. Roof-crush strength improvement using rigid polyurethane foam. J Mater Eng Perform 1998;7(4):511–4.

[55] Chopra AK. Dynamics of structures- theory and applications to earthquake engineering. Upper Saddle River (NJ, USA): Prentice Hall; 2012.